PHYSICAL REVIEW RESEARCH **4**, 023022 (2022)

Multi-photon multi-quantum transitions in the spin-$\frac{3}{2}$ silicon-vacancy centers of SiC

Harpreet Singh,[1,*] Mario Alex Hollberg,[1] Andrey N. Anisimov,[2] Pavel G. Baranov,[2] and Dieter Suter[1]
[1]*Fakultät Physik, Technische Universität Dortmund, D-44221 Dortmund, Germany*
[2]*Ioffe Institute, St. Petersburg 194021, Russia*

(Received 20 December 2021; accepted 9 March 2022; published 8 April 2022)

Silicon vacancy centers in silicon carbide are promising candidates for storing and manipulating quantum information. Implementation of fast quantum gates is an essential requirement for quantum information processing. In a low magnetic field, the resonance frequencies of silicon vacancy spins are in the range of a few MHz, the same order of magnitude as the Rabi frequencies of typical control fields. As a consequence, the rotating wave approximation becomes invalid and nonlinear processes like the absorption and emission of multiple photons become relevant. This paper focuses on multi-photon transitions of negatively charged silicon vacancies driven by a strong RF field. We present continuous-wave optically detected magnetic resonance (ODMR) spectra measured at different RF powers to identify the 1-, 2-, and 3 RF photon transitions of different types of the silicon vacancy in the 6H-SIC polytype. Time-resolved experiments of Rabi oscillations and free induction decays of these multiple RF photon transitions were observed. Apart from zero-field data, we also present spectra in magnetic fields with different strength and orientation with respect to the system's symmetry axis.

DOI: 10.1103/PhysRevResearch.4.023022

I. INTRODUCTION

Vacancies in silicon carbide (SiC) are excellent candidates for quantum sensing and technology applications [1–5] as they can be controlled coherently and have long spin coherence times [6–8]. Apart from that, mature fabrication techniques exist for SiC. Here we focus on the silicon vacancies in the 6H-SiC polytype [9–11], where three types of Si vacancies have been identified, labeled V_1, V_2, and V_3, which correspond to different lattice positions [4,12,13]. It has been shown that silicon-vacancies at hexagonal sites h corresponds to V_1, while V_3 and V_2 are at cubic lattice sites k_1 and k_2 [14]. When the vacancies are negatively charged (V_{Si}^-), they have spin 3/2 and the ground state spin sublevels can be polarized by optical irradiation [10,11]. In previous papers, we measured relaxation rates and optical spin initialization of V_{Si}^- at room temperature [9,10], the polarization dependencies of the ZPLs and the ODMR contrast as a function of temperature [15].

V_{Si}^- in 6H-SiC have smaller crystal field splittings than nitrogen vacancies in diamond. Even at modest radio frequency (RF) powers, the spin Rabi frequencies are in the MHz range and thus comparable to the resonance frequency in zero or low magnetic field. Hence, the RF field drives not only the allowed single-photon transitions, but we also find absorption of multiple photons, aperiodic evolution of the system and nonlinear dependencies of effective Rabi frequencies on the applied RF strength. A multi-photon transition occurs by simultaneous absorption and emission of multiple photons such that the transition frequency corresponds to an integer multiple of the driving RF frequency [16–20]. Two-photon transitions have been studied in different systems [21–24] including NMR of spin-1 system [25]. The two RF photon absorption between two spin states differing by $\Delta m_S = 2$ has also been observed in V_{Si}^- [8]. Further, the absorption of a single photon causing a weak transition with $\Delta m_S = 2$ was also observed in the V_2 type vacancies of 4H-SiC [26]. The authors mentioned as a possible cause of these transitions stray magnetic fields not aligned with the c axis or the hyperfine interaction of the V_{Si}^- with nuclear spins, which lead to a mixing spin levels and make the double quantum transitions, which are normally forbidden, weakly allowed. Later, it has been demonstrated that the amplitude of the double-quantum transitions of V_{Si}^- was the same in natural and isotopically purified 4H-SiC samples [27]. These authors considered additional terms in the spin Hamiltonian due to the trigonal pyramidal symmetry of this center as the cause of these double-quantum spin transitions [27].

Figure 1 shows a typical experimental spectrum of the V_3 vacancy in magnetic field of 4.5 mT ∥ c axis with a number of transitions that do not match the "allowed" magnetic dipole transitions. The resonances marked with 1 and 2, which are found at the lowest frequencies, are 3-photon transitions between spin states with $\Delta m_s = 1$ while peaks 5 and 6 are due to the 2-photon transitions between spin levels with $\Delta m_s = 2$. The peak labeled with 7 in Fig. 1 is due to a single-photon, 2-quantum transition between the spin levels $3/2 \leftrightarrow -1/2$.

This paper explores the possible multi-photon and multiple quantum transitions of the V_{Si}^- in the 6H-SiC using continuous wave and pulsed ODMR techniques. We numerically simulate

---

[*] harpreet.singh@tu-dortmund.de

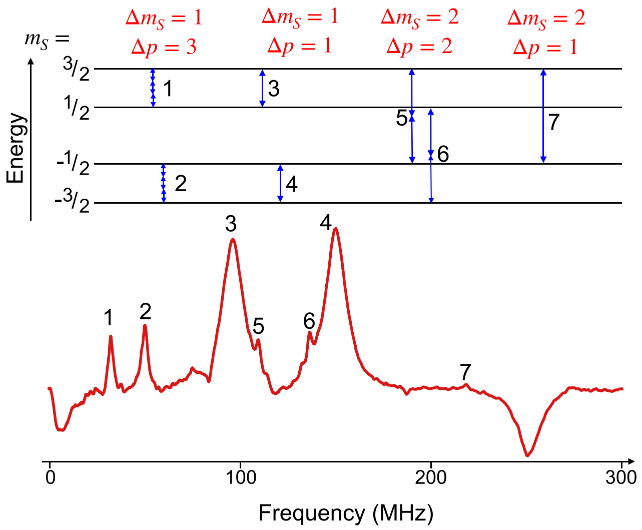

FIG. 1. ODMR spectrum and energy level diagram of the spin states of V_3 in a 4.5-mT magnetic field ∥ to the c axis with different types of multiple photon and multiple quantum transitions. Δm_s and Δp are the changes in spin angular momentum and the number of absorbed RF photons for each transition

the stationary and time-dependent system response through a master equation for the V_{Si}^- spin ensemble. The results are in excellent agreement with the experimental observations.

This paper is organized as follows. Section II introduces the properties of the spin system. The first subsection of Sec. III provides some details about continuous-wave optically detected magnetic resonance (cw-ODMR) experiments at different RF powers. The second subsection shows time-resolved measurements of 1-, 2-, and 3 RF photon transitions. Section IV provides some details about the simulations. Section V A contains the ODMR recorded in the presence of magnetic fields. Finally, Sec. VI contains a brief discussion and some concluding remarks.

II. SYSTEM

The experiments reported here were performed on an ensemble of V_{Si}^- in a 6*H*-SiC sample, and details of the sample preparation are given in Appendix A. The site symmetry of the V_{Si}^- center is C_{3v} and the electronic spin is $S = 3/2$. The spin Hamiltonian is

$$\mathcal{H} = D\left(S_z^2 - \frac{S(S+1)}{3}\right) + g\mu_B \vec{B}\cdot\vec{S}, \tag{1}$$

where the zero field splitting (ZFS) in the electronic ground state is $2D = 128$ MHz, in frequency units ($h = 1$) for V_2 and –28 MHz for V_3 [1]. $g = 2$ is the electron g factor, μ_B is the Bohr magneton, $\vec{B}$ is the applied static magnetic field and $\vec{S} = \{S_x, S_y, S_z\}$ is the vector of spin operators.

We drive the evolution of the electron spins by a sinusoidally oscillating RF field. For a field perpendicular to the symmetry axis, the interaction Hamiltonian between the RF field and the spins is

$$\mathcal{H}_{\mathrm{RF}}(t) = \Omega_1(\cos\varphi\cos(2\pi\omega t)\,S_x + \sin\varphi\sin(2\pi\omega t)\,S_y), \tag{2}$$

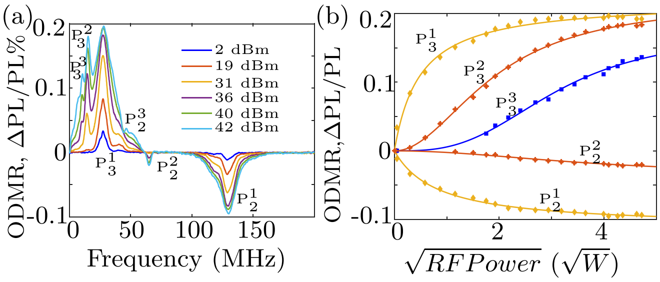

FIG. 2. (a) Experimental ODMR spectra at different power levels. (b) Amplitudes of the different peaks vs RF field strength.

where $\Omega_1 = g\mu_B B_1$ represents the strength of the coupling to the RF field B_1 in frequency units, ω is the oscillation frequency of the field and the angle φ parametrises the polarization of the RF field: for $\varphi = n\pi/2$, n integer, the field is linearly polarized, other values correspond to elliptical (including circular) polarization.

When the V_{Si}^- are irradiated with a suitable wavelength laser, population is transferred to the excited state. Most of the population falls back to the ground state by spontaneous emission, but some of it undergoes intersystem crossing (ISC) to the shelving states and preferentially returns to specific ground-state spin-levels depending upon the type of vacancies [4,9,28]: In V_2 (V_3), the population preferentially falls into the ±3/2 (±1/2) spin states [10].

Another process that affects the dynamics of the silicon-vacancy is spin relaxation: spin-lattice (T_1 relaxation) and spin-spin relaxation (T_2 relaxation). We studied these relaxation processes at room temperature and determined the corresponding relaxation rates in previous papers [9,10].

III. OPTICALLY DETECTED MAGNETIC RESONANCE

Optically detected magnetic resonance (ODMR) is a technique for measuring electron spin resonance (ESR) through an optical signal instead of inductive detection [29,30]. The optical irradiation establishes a non-thermal population of the different spin states. Since the different spin states contribute differently to the photoluminescence (PL) rate, a change in the spin polarization leads to a change of the PL rate, which can be used to measure the spin polarization. The sensitivity of this technique is often high enough to measure ODMR of individual electron spins [2,30–32]. We used the same technique for measuring the ODMR of silicon vacancies in 6H-SiC with natural isotopic composition. Additional details of the ODMR setup are given the Appendix B.

A. Continuous-wave ODMR

In our continuous-wave (CW) ODMR experiments, the sample was continuously illuminated with 785-nm laser light while the RF field was modulated (switched ON / OFF). The PL from the sample was collected and detected by an avalanche photodiode (APD) module after passing through a 850-nm long-pass filter. The electrical signal from the APD was recorded by a lock-in amplifier referenced to the ON/OFF modulation signal [9,10]. Figures 1 and 2(a) show two such spectra, which were recorded at room temperature,

TABLE I. Fitting parameters of Eq. (3) for the different ODMR peaks $P_2^{i=1,2}$ and $P_3^{i=1,2,3}$ of the V_2 and V_3 vacancies.

V_{Si}^-	Peaks	c	$S_{max}(\%)$	$\Lambda_0(W^{c/2})$
V_2	P_2^1 (128 MHz)	1	-0.111 ± 0.004	0.825 ± 0.117
V_2	P_2^2 (64 MHz)	2	-0.037 ± 0.007	14.92 ± 5.34
V_3	P_3^1 (28 MHz)	1	0.219 ± 0.006	0.488 ± 0.076
V_3	P_3^2 (14 MHz)	2	0.218 ± 0.004	3.693 ± 0.236
V_3	P_3^3 (9 MHz)	3	0.171 ± 0.008	28.92 ± 3.59

in a field of 4.5 mT (Fig. 1) and 0 [Fig. 2(a)], respectively, by recording the lock-in signal as a function of the RF frequency. At low RF power, two peaks are visible in the zero-field spectrum of Fig. 2(a), a positive one at 28 MHz (P_3^1) and a negative one at 128 MHz (P_2^1), which correspond to the V_3 and V_2 sites of V_{Si}^-. A positive signal corresponds to an increase in the PL when the RF field is resonant. As the RF power is increased, the amplitude and width of these peaks increases and additional peaks become visible at 9 MHz (P_3^3), 14 MHz (P_3^2), 43 MHz (P_2^3), and 64 MHz (P_2^2). The resonance lines marked P_3^3 (P_3^2) and P_2^3 (P_2^2) appear at one-third and one-half to the frequency of the V_3 (V_2) peaks. The peak P_2^3 at 43 MHz overlaps with P_3^1.

The different peaks show remarkably different power dependence as shown in Fig. 2(b), which represents the ODMR signal amplitude vs. the square root of the applied RF power of all peaks except P_2^3 (which is difficult to extract, due to the overlap). The experimental data were fitted with the function

$$S(\Lambda) = S_{\max}[\Lambda^c/(\Lambda_0 + \Lambda^c)], \tag{3}$$

where $S(\Lambda)$ is the ODMR signal amplitude and Λ the square root of RF power. The exponent c is set to 1, 2, and 3 for the 1-, 2-, and 3-photon transitions. If the exponent c is used as an additional fitting parameter, the optimal fit is obtained with values that are close to these. The values for S_{max} and Λ_0 for the different peaks are given in Table I.

B. Time-resolved experiments

For measuring Rabi oscillations and free induction decays with 1-, 2-, and 3 RF photon excitation, we used time-resolved ODMR. A typical time-resolved ODMR experiment consists of an initial laser pulse, which polarizes the spin ensemble. Then, a set of RF pulses and delays are applied before measuring the PL with a measuring laser pulse. We will start with the Rabi oscillation.

1. Rabi oscillations

Figure 3(a) shows the pulse sequence for measuring Rabi oscillations for the different transitions. The spin ensemble was first polarized with a 300 μs laser pulse. A signal was recorded during a 4 μs laser pulse after an RF pulse of variable duration τ_R. The same experiment was repeated without the RF pulse to obtain a reference signal to suppress background signals. The signals obtained from both experiments were subtracted from each other for each pulse duration τ_R [9,10]. Figure 3(b) shows the Rabi oscillation recorded in zero magnetic field for the V_3 type with 1-, 2-, and 3 RF photon transitions at room temperature. For measuring Rabi oscillations of the 1 photon transition, a 28-MHz linearly polarized RF pulse of 11 W was applied, whereas 14 MHz (9.3 MHz) was used for the 2 (3) photon transition with the same RF power. The red curves in Fig. 3(b) are signals calculated for the 1 photon (ω = 28 MHz), 2 photon (ω = 14 MHz), and 3 photon (ω = 9.3 MHz) transitions. More details about the simulations of the curves are given in Sec. IV A.

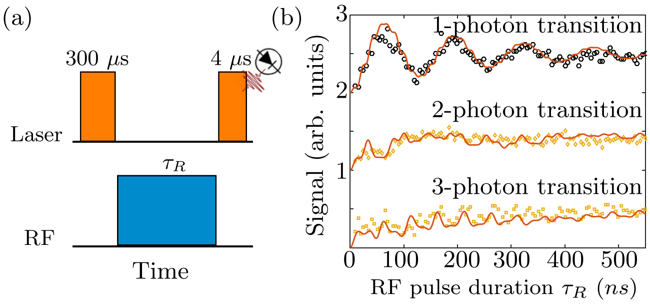

FIG. 3. (a) Pulse sequence for measuring Rabi oscillations. (b) Rabi oscillations measured for V_3 with 1-, 2-, and 3 RF photons at room temperature. Circles, diamonds and squares represent experimentally measured data. Red curves are the simulations obtained by solving Eq. (7) numerically for different photons transitions. The curves have been shifted vertically to avoid overlap.

2. Free Induction Decay

Figure 4(a) shows the pulse sequence for measuring free induction decays (FIDs). As above, we initialized the spin ensemble by a first laser pulse and a first RF pulse with a frequency of 28 MHz, 14 MHz, and 9.3 MHz for 1-, 2-, and 3 photon transitions and duration 25 ns for all cases. During the subsequent delay τ_f, the coherence generated by the pulse was allowed to precess freely. A second RF pulse with the same frequency and duration, and phase $\phi_d = 2\pi f_{\text{det}} \tau_f$ (detuning frequency f_{det} = –40 MHz) was applied before the readout laser pulse. We again used the difference between two experiments, where the second RF pulses have phases ϕ_d and $\phi_d + \pi$, respectively, to suppress unwanted background signals [9,10]. Figure 4(b) shows the experimentally recorded

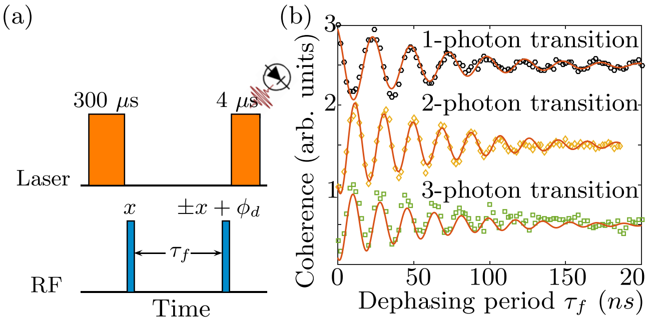

FIG. 4. (a) Pulse sequence for measuring FIDs. (b) FIDs measured for V_3 with 1-, 2-, and 3 RF photons in zero magnetic field at room temperature. Circles, diamonds, and squares represent experimentally measured data. Red curves were obtained by fitting the experimental data to the fitting function given in Eq. (4). The curves have been shifted vertically to avoid overlap.

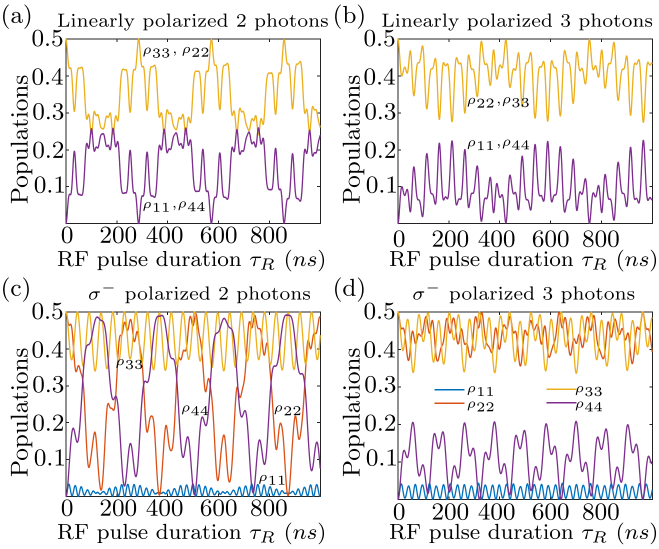

FIG. 5. Simulation of population dynamics of the V_3 vacancy with linearly polarized RF excitation for (a) 2 photons (14 MHz), (b) 3 photons (9.3 MHz), left circularly (σ^-) polarized (c) 2 photons (14 MHz), and (d) 3 photons (9.3 MHz).

FIDs with the 1-, 2-, and 3 RF photon pulses in zero magnetic field and at room temperature. The recorded experimental data were fitted with the function:

$$S^N_{x+\phi_d} - S^N_{-x+\phi_d} = A\cos(2\pi f - \phi)\, e^{-\tau_f/T_2^*}, \tag{4}$$

where $S^N_{x+\phi_d}$ and $S^N_{-x+\phi_d}$ are signals recorded with N-photon pulses in the main and reference experiment. The values obtained for the frequency f are 40.0 ± 0.1 MHz, 53.3 ± 0.2 MHz, and 56.1 ± 0.5 MHz for 1-, 2-, and 3 photon FID measurements respectively; and the average dephasing rate T_2^* is 62.0 ± 5.6 ns. In these experiments, the signal frequency f is the difference between the transition frequency ($2D = 28$ MHz) and the sum of the RF frequency f_{RF} and the detuning frequency f_{det} : $f = |2D - (f_{\mathrm{RF}} + f_{\mathrm{det}})|$.

IV. SPIN DYNAMICS

The dynamics of the closed spin system can be estimated using the Liouville–von Neumann equation:

$$\frac{\partial \rho}{\partial t} = -2\pi i\, [\mathcal{H}_t(t), \rho], \tag{5}$$

where we use units with $h = 1$, ρ is the spin density matrix, $\mathcal{H}_t(t) = \mathcal{H} + \mathcal{H}_{\mathrm{RF}}(t)$ is the total Hamiltonian, i.e., the sum of the static system Hamiltonian $\mathcal{H}$ given in Eq. (1) and the time-dependent RF Hamiltonian $\mathcal{H}_{\mathrm{RF}}(t)$ in the laboratory frame, which is given in Eq. (2). We solve it numerically using the Runge-Kutta 4 method, without invoking the rotating wave approximation to include higher-order contributions.

A. Coherent Evolution

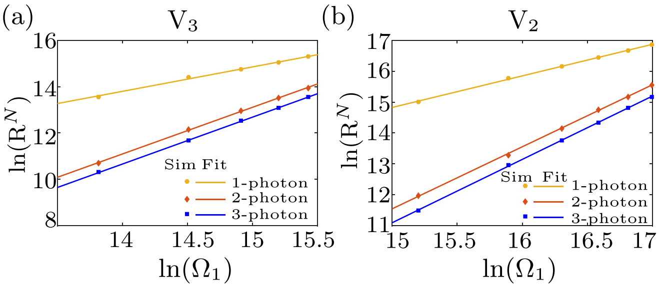

FIG. 6. Log of Rabi frequency of N-photon transitions vs log of RF coupling strength Ω_1 for (a) V_3 and (b) V_2.

Figure 5 shows the simulation results obtained using Eq. (5) (ignoring relaxation processes), with a diagonal initial state $\rho_0 = \{0, 0.5, 0.5, 0\}$, RF coupling strength $\Omega_1 = 9.1$ MHz, using the RF Hamiltonian given in Eq. (2) with $\phi = 0$ for linear and $\phi = \pi/4$ for left circular (σ^-) polarized RF. Figures 5(a) and 5(b) shows the population dynamics of V_3 with the absorption of 2 ($\omega = 14$ MHz) and 3 ($\omega = 9.3$ MHz) linearly polarized RF photons, respectively. In comparison, Figs. 5(c) and 5(d) shows the population dynamics for the system interacting with a left circularly (σ^-) polarized RF field resonant with the 2- and 3- photon transitions. The circularly polarised field breaks the symmetry observed in Figs. 5(a) and 5(b) by exciting mostly the spin transition $1/2 \leftrightarrow -3/2$ with $\Delta m_S = 2$ in the case of 2-photon absorption and the transitions $1/2 \leftrightarrow -3/2$ and $-1/2 \leftrightarrow -3/2$ with $\Delta m_S = 2$ and $\Delta m_S = 1$ in the case of 3-photon excitation. This is in contrast to the linearly polarized field, which couples equally to $1/2 \leftrightarrow -3/2$ and $-1/2 \leftrightarrow 3/2$.

Since the strength of the RF field is comparable to the transition frequency, the relation between field strength and the observed dynamics is highly nonlinear. As shown in Fig. 5, the oscillations of the populations contain multiple frequencies. Fourier-transformation shows that they consist of a small number of frequencies whose amplitudes and positions shift with increasing RF field strength. As a comparison with typical resonant excitations (Rabi-flopping), we perform Fourier transforms of the time-traces and consider the main frequency component as the Rabi frequency. For the data of Fig. 5, the extracted Rabi frequencies are 7.8 MHz, 3.39 MHz, and 2.56 MHz for 1-, 2-, and 3-photon transitions. In Fig. 6, we show additional data for different RF field strengths in log-log plots. The individual data points are fitted to straight lines,

$$ln\ R_N = a\ ln\ \Omega_1 + b. \tag{6}$$

The fitting parameters a and $\boldsymbol{b}$ are given in Table II.

B. Relaxation

The V_{Si}^- spin ensemble continuously interacts with its environment, which causes relaxation. This system-environment

TABLE II. Fitting parameters of Eq. (6).

	log-log fitting			
	V_3		V_2	
N	a	b	a	b
1	1.05±0.10	−0.95±1.55	1.02±0.03	−0.47±0.51
2	2.01±0.05	−17.07±0.77	2.00±0.08	−18.51±1.35
3	2.02±0.02	−3.52±0.30	2.05±0.02	−19.59±0.35

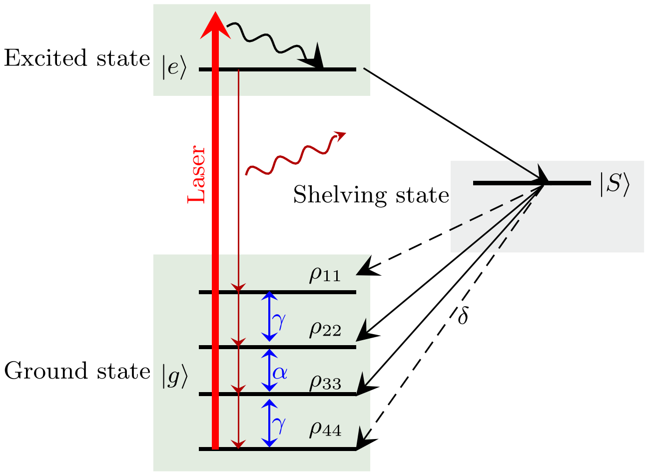

FIG. 7. Simplified energy-level diagram of V_{Si}^-, indicating optical pumping and relaxation processes. The ground, excited, and shelving states are labeled $|g\rangle$, $|e\rangle$, and $|s\rangle$. The nonresonant laser excitation is shown with a red arrow.

interaction has two main effects on the system, which is not in its thermal equilibrium state. The first is the loss of coherence, also called spin-spin relaxation, which preserves the energy of the system. It can be taken into account by a term $\dot{\rho}_{ik} = -\rho_{ik}/T_2^{ik}$ in the equation of motion. The second effect is that the populations relax back to thermal equilibrium by a process called spin-lattice relaxation. In this process, energy is exchanged between the system and its environment (the lattice) [33]. This contribution can be taken into account as $\dot{\vec{p}} = M\vec{p}$, where the population vector $\vec{p}$ includes the diagonal density operator elements and the transition matrix M depends on the mechanism that couples the system to the environment. Here, we assume that the spin levels 1/2 and –1/2 equilibrate with a rate α and spin levels $\pm 3/2$ and $\pm 1/2$ equilibrate with a rate γ. This corresponds to the transition matrix

$$M = \begin{pmatrix} -\gamma & \gamma & & \\ \gamma & -\alpha-\gamma & \alpha & \\ & \alpha & -\alpha-\gamma & \gamma \\ & & \gamma & -\gamma \end{pmatrix}.$$

In our previous paper [9], we determined these spin relaxation rates for the V_1 type of V_{Si}^- and found that the ratio α/γ agrees with the theoretical value of 4/3. We also studied the dynamics of the optical initialization process and found that the laser illumination transfers the population from $\pm 3/2$ to $\pm 1/2$ with a pumping rate δ, which is proportional to the laser intensity [9]. Figure 7 shows the optical pumping and relaxation schemes used for the silicon vacancies. The ground, excited, and shelving states are labeled $|g\rangle$, $|e\rangle$, and $|s\rangle$. The nonresonant laser excitation is shown with a thick red arrow. When the vacancy is excited with the laser light, most of the population falls back from the electronically excited state to the ground state by spontaneously emitting photons. The system can also undergo ISC to the shelving states, from where it preferentially relax to the spin levels $\pm 1/2 (\pm 3/2)$ of the electronic ground state in case V_3 (V_2). An optical pumping rate δ is the rate at which population is pumped from the electronic ground-state spin levels $\pm 3/2$ to $\pm 1/2$ in case of V_3 and vice versa for V_2 [9,10].

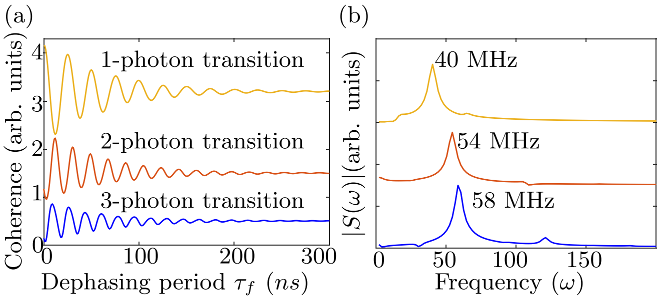

FIG. 8. (a) Simulated FIDs for 1-, 2-, and 3 photon excitation using Eq. (7), and (b) Fourier transform of the simulated FID signals.

For the numerical simulation, we use the Lindblad master equation

$$\frac{\partial \rho}{\partial t} = -2\pi i\,[\mathcal{H}_t(t), \rho] + \sum_{\alpha,\beta,\delta_{1,..,5}} L_i^\dagger.\rho.L_i - \frac{1}{2}\{L_i^\dagger L_i, \rho\} \tag{7}$$

here $L_\alpha = \sqrt{2}\begin{pmatrix} 0 & \sqrt{\gamma} & 0 & 0 \\ \sqrt{\gamma} & 0 & \sqrt{\alpha} & 0 \\ 0 & \sqrt{\alpha} & 0 & \sqrt{\gamma} \\ 0 & 0 & \sqrt{\gamma} & 0 \end{pmatrix} \approx \sqrt{2\alpha}\,S_x$ (taking into account $\gamma = 3\alpha/4$) drives the spin-lattice relaxation process, $L_\beta = \sqrt{2\beta}\,S_z$ is the Lindblad operator for the dephasing process, and $L_{\delta_{1,\dots,5}}$ are the Lindblad operators for the optical pumping. The matrix forms of the other Lindblad operators are given in Appendix C.

The red curves in Fig. 4(b) of Sec. III B 1 are signals calculated as 0.5(1+ρ_{11}-ρ_{22}-ρ_{33}+ρ_{44}) from Eq. (7) for 1 photon- (ω = 28 MHz), 2 photon- (ω = 14 MHz), and 3 photon- (ω = 9.3 MHz) transitions, with an initial diagonal state $\rho_0 = \{0, 0.5, 0.5, 0\}$, RF coupling strength $\Omega_1 = 9.1$ MHz, using the RF Hamiltonian given in Eq. (2) with $\phi = 0$ for a linearly polarized RF field and using the Runge-Kutta 4 method. Additional details are given in Appendix C. To simulate the effect of RF inhomogeneity, signals with 0.97, 1, and 1.03 times Ω_1, were calculated and added with weights 0.3, 0.4, and 0.3, respectively. The values of the relaxation rate was $\alpha = 1/107\ \mu s^{-1}$ and for the dephasing rate $\beta = 1/148\,\text{ns}^{-1}$, $1/500\,\text{ns}^{-1}$, and $1/1000\,\text{ns}^{-1}$ for the 1-, 2-, and 3-photon excitation.

Figure 8 shows the simulated FIDs for the 1-, 2-, and 3 RF photon excitation using Eq. (7) with a diagonal, spin-lattice relaxation rate $\alpha = 1/107\,\mu s^{-1}$. For the FID simulations, we used an initial state $\rho_0 = \{0, 0.5, 0.5, 0\}$ to which we applied a 25-ns RF pulse by letting the system evolve under the total Hamiltonian $\mathcal{H}_t(t) = \mathcal{H} + \mathcal{H}_{\text{RF}}(t)$, with the RF coupling strength $\Omega_1 = 9.1$ MHz. The resulting state was allowed to evolve for a time τ_f under the system Hamiltonian $\mathcal{H}$, with the dephasing rate $\beta = 1/62\ \text{ns}^{-1}$. After the free evolution, the second RF pulse was applied, with the phase $\phi_d = 2\pi f_d \tau_f$ ($f_d = -40$ MHz). The resulting signal was calculated from the final density matrix elements as $S_{x+\phi_d}^N = \rho_{11} - \rho_{22} - \rho_{33} + \rho_{44}$. Similarly the reference signal $S_{-x+\phi_d}^N$ was calculated by adding an extra π phase in the RF Hamiltonian of the second pulse. The difference signal $S_{x+\phi_d}^N - S_{-x+\phi_d}^N$ is plotted

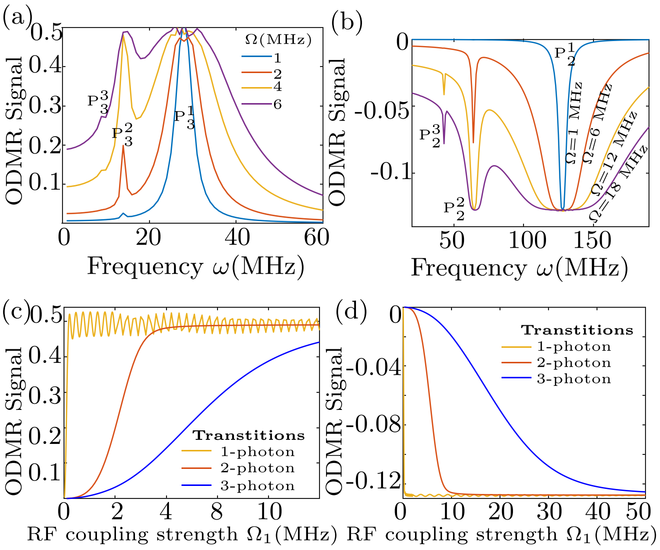

FIG. 9. Simulated ODMR signal vs frequency ω at different RF coupling strength Ω_1 for (a) V_3, (b) V_2. ODMR signal of 1-, 2-, and 3-photon peaks vs RF coupling strength for (c) V_3, (d) V_2.

in Fig. 8(a) while Fig. 8(b) shows the corresponding Fourier transforms (FFTs) for the 1-, 2-, and 3 RF photon excitation. The main resonance lines are found at $f = |2D - (f_{\rm RF} + f_{\rm det})|$, in agreement with the experimental data.

C. CW ODMR

The data in Sec. III A clearly show that 1-, 2-, and 3-photon transitions show different dependence on the RF power. It is therefore essential to model the system dynamics under different RF power levels and in constant laser light. To obtain the CW ODMR spectra, we integrated the master equation with the total Hamiltonian $\mathcal{H}_t(t) = \mathcal{H} + \mathcal{H}_{\rm RF}(t)$ for 4 μs and plotted the resulting signal as a function of the RF frequency. The ODMR signal was calculated as the difference $S_{\rm RF} - S_0$ between the signal $S_{\rm RF}$ with applied RF field and the reference signal S_0. Each part was calculated from the diagonal elements of the stationary density matrix as $S_{\rm RF} = \rho_{11} - \rho_{22} - \rho_{33} + \rho_{44}$ [9,34], where ρ_{11}, ρ_{44}, and ρ_{22}, ρ_{33} are the populations of the spin levels$|\pm 3/2\rangle$ and $|\pm 1/2\rangle$, respectively.

Figure 9(a) shows the simulated ODMR signal at different RF coupling strengths Ω_1 vs RF frequency ω obtained by numerically solving Eq. (7) with a diagonal initial state $\rho_0 = \{\frac{\gamma}{4(\gamma+\delta)}, \frac{\gamma+2\delta}{4(\gamma+\delta)}, \frac{\gamma+2\delta}{4(\gamma+\delta)}, \frac{\gamma}{4(\gamma+\delta)}\}$ ($\{\frac{\gamma+2\delta}{4(\gamma+\delta)}, \frac{\gamma}{4(\gamma+\delta)}, \frac{\gamma}{4(\gamma+\delta)}, \frac{\gamma+2\delta}{4(\gamma+\delta)}\}$ for V_2) where $\gamma = \frac{3}{4}\alpha$, for time $t = 0$ to 4 μs in 8000 time steps, using the RF Hamiltonian given in Eq. (2) with $\phi = 0$ for a linearly polarized RF field. The rates α, β, and δ were extracted from experimental data: The spin-lattice relaxation rate is $\alpha = 10.8$ ms^{-1} (9.3 ms^{-1}) for $V_2(V_3)$, as determined in our earlier papers [9,10]. Under the influence of an RF field, the dephasing is slower than during free precession and depends on the homogeneity of the RF field. We therefore estimated it from the Rabi measurements at different RF powers. For low power, the dephasing rate decreases linearly with increasing RF power and then increases linearly in both types of vacancies. This indicates that the RF field decouples the vacancy spin from nuclear spins coupled by hyperfine interactions, while at higher power, the effect of RF inhomogeneity starts to dominate. Further, the dephasing rate also depends on the applied static magnetic field to the V_{Si}^- [26]. For our calculation, we took the smallest observed dephasing rate $\beta \approx 2.5\,\mu$s^{-1}(1.3 μs^{-1}) for $V_2(V_3)$ to optimize the resolution. The pumping rate $\delta = 1.4$ ms^{-1}(6.8 ms^{-1}) for $V_2(V_3)$ was extracted from the time-dependence of the PL signal measured after an RF pulse of 20 μs using the model described in Ref. [9]. Figure 9(b) shows the ODMR signal for the 1-, 2-, and 3 RF photon peaks vs the RF field strength Ω_1. In the simulated ODMR spectra of the V2 and V3 vacancies, the 1-, 2-, and 3 RF photons absorption peaks are visible. The intensity of peak P_3^3 (3 RF photon transition) is small relative other two peaks as compared to the experimental recorded spectra and we will address this in Sec. V C.

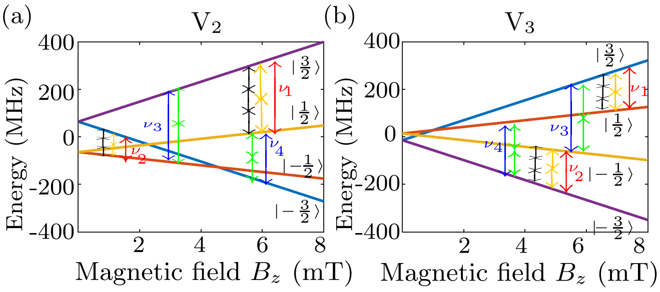

FIG. 10. Energy levels of (a) the V_2 vacancy and (b) V_3 vacancy in a magnetic field parallel to crystal c axis. Arrows represent the possible transitions. Red and blue arrows are for the one-photon transitions; green and yellow arrows are for the two-photon transitions; and black arrows are for the three-photon transitions.

V. ODMR IN A MAGNETIC FIELD

While the experiments described in the preceding sections were performed in zero field, we now consider the effect of magnetic fields. In Sec. V A, we consider fields applied parallel to the symmetry axis of the center lifts the degeneracy of the energy levels as well of the transitions. This is particularly relevant as it allows one to distinguish between single- (e.g., $+1/2 \leftrightarrow +3/2$) and multiple quantum transitions (e.g., $-1/2 \leftrightarrow +3/2$) that are degenerate in zero field but behave differently. In Sec. V B, we also consider fields not aligned with the symmetry axis, which modify not only the transition frequencies but also the transition probabilities.

Figures 10(a) and 10(b) show the energy levels of V_2 and V_3 types of vacancies in an external magnetic field parallel to the crystal c axis along with different types (multiple photon / multiple quantum observe in the experiment) transitions. The red arrows labeled with ν_1 and ν_2 represent the allowed single-quantum transition from $|3/2\rangle \leftrightarrow |1/2\rangle$ and $|-3/2\rangle \leftrightarrow |-1/2\rangle$, respectively. The blue arrows labeled with ν_3 and ν_4 represent the two-quantum transitions from $|3/2\rangle \leftrightarrow |-1/2\rangle$ and $|-3/2\rangle \leftrightarrow |1/2\rangle$, respectively.

In Appendix C, Fig. 15 shows different possible transitions for the V_1/V_3 and V_2 for a range of magnetic fields B ∥ c axis, calculated using eigenvalues of Hamiltonian given in Eq. (1).

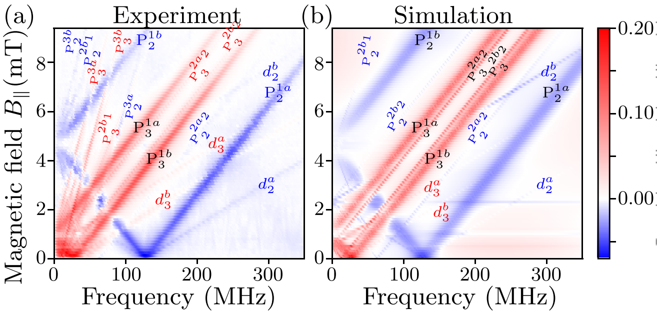

FIG. 11. (a) Experimental, and (b) simulated ODMR spectra for a range of magnetic fields $B \parallel c$ axis showing different possible transitions for V_1/V_3 and V_2. Peaks labeled with $P_2^{1a(b)}$ ($P_3^{1a(b)}$), $P_2^{2a(b)}$ ($P_3^{2a(b)}$) and $P_2^{3a(b)}$ ($P_3^{3a(b)}$) are 1, 2 and 3 RF photons absorption peaks due to the single quantum spin transition $\Delta m_s = 1$, peaks $d_2^{a(b)}(d_3^{a(b)})$ are 1 RF photon absorption peaks due to double quantum spin transition $\Delta m_s = 2$ for $V_2(V_3)$ type of V_{Si}^-. The color scale is in units of ΔPL/PL%.

A. Magnetic field parallel to the *c* axis

Figure 11(a) shows the ODMR recorded in an external magnetic field parallel to the c axis using an RF power of $\approx$ 5 W at room temperature. A peak $P_{i=2,3}^{1a(b)}$ is due to the 1 RF photon transition between the levels $3/2 \leftrightarrow 1/2$ $(-3/2 \leftrightarrow -1/2)$ of the $V_{i=2,3}$ type of V_{Si}^-. Peaks labeled with 3 and 4 in Fig. 1 are 1 RF photon transition between $3/2 \leftrightarrow 1/2$ and $-3/2 \leftrightarrow -1/2$ of V_3. Peaks $P_i^{2a_1(b_1)}$ are due to the absorption of 2 RF photons between the spin levels $3/2 \leftrightarrow 1/2(-3/2 \leftrightarrow -1/2)$ [as shown in Figs. 10(a) and 10(b) with two yellow arrows] and appear at half the corresponding transition frequency. Another 2 RF photon peaks $P_i^{2a_2(b_2)}$ are due to absorption of 2 photons between the spin levels $3/2 \leftrightarrow -1/2(-3/2 \leftrightarrow 1/2)$ as shown in Figs. 10(a) and 10(b) with two green arrows. Peaks labeled with 5 and 6 in Fig. 1 are 2 RF photons transition between $3/2 \leftrightarrow -1/2$ and $-3/2 \leftrightarrow 1/2$ of V_3. A peak $P_i^{3a(b)}$ is due to the absorption of 3 RF photons between the spin levels $3/2 \leftrightarrow 1/2(-3/2 \leftrightarrow -1/2)$ [as shown in Figs. 10(a) and 10(b) with three black arrows] and appears at one third of the corresponding transition frequency. Peaks labeled with 1 and 2 in Fig. 1 are 3 RF photons transition between $3/2 \leftrightarrow 1/2$ and $-3/2 \leftrightarrow -1/2$ of V_3. The slope of 2- and 3-photon transition between the levels $\pm 3/2 \leftrightarrow \pm 1/2$ is 2 and 3 times higher than the slope of the 1-photon transition. Additional peaks $d_{i=2,3}^a$ and $d_{i=2,3}^b$ for $V_{i=2,3}$ type of V_{Si}^- are due to the absorption of 1 RF photon by spin levels $\pm 3/2 \leftrightarrow \mp 1/2$. This type of transitions were also seen previously for the V_2 type of vacancies in 4*H*-SiC, and the authors suggested that the cause of these transitions was the fine structure of the V_2 vacancy [27,35]. Details of these peaks are given in Table III. Figure 11(b) shows the corresponding simulated spectra for an external magnetic field almost parallel (angle of inclination is 2.5°) to the c axis, obtained by numerically solving Eq. (7) using the same method and relaxation and pumping parameters are given in the above Sec. III A. The applied magnetic field removes the degeneracies in the spin levels. For some magnetic field values, level-anticrossing also happens, so the reference signal S_0 was calculated from the diagonal elements of the stationary density matrix without RF for a particular magnetic field. The obtained ODMR signal was renormalized to match the experimental signal and plotted. The RF Strength Ω_1 used for both vacancies was 6 MHz. In the simulations, 1- and 2- photon peaks are visible along with the 1 RF photon absorption peaks $d_{i=2,3}^{a(b)}$ by spin levels $\pm 3/2 \leftrightarrow \mp 1/2$ of $V_{i=2,3}$ type of V_{Si}^-.

TABLE III. Detail of Fig. 11 peak labels and their correspondence to the spin transition levels. Δm_s and Δp are the changes in spin angular momentum and the number of absorbed RF photons for each transition and $m = (g\mu_B)^{-1}$.

Peak	Δp	Δm_s	Slope $B_\parallel/\omega$	Transition
$P_{i=2,3}^{1a(b)}$	1	1	m	$3/2 \leftrightarrow 1/2\ (-3/2 \leftrightarrow -1/2)$
$d_{i=2,3}^{a(b)}$	1	2	$0.5m$	$3/2 \leftrightarrow -1/2\ (-3/2 \leftrightarrow 1/2)$
$P_{i=2,3}^{2a_1(b_1)}$	2	1	$2m$	$3/2 \leftrightarrow 1/2\ (-3/2 \leftrightarrow -1/2)$
$P_{i=2,3}^{2a_2(b_2)}$	2	2	m	$3/2 \leftrightarrow -1/2\ (-3/2 \leftrightarrow 1/2)$
$P_{i=2,3}^{3a(b)}$	3	1	$3m$	$3/2 \leftrightarrow 1/2\ (-3/2 \leftrightarrow -1/2)$

B. Magnetic field with component perpendicular to the *c* axis

The simulated ODMR of magnetic field small with c axis enables the double quantum transitions $d_{i=2,3}^{a(b)}$. It is interesting to see the effect of B perpendicular to the c axis. Figure 12(a) shows the ODMR recorded in different magnetic fields $\perp$ to the c axis in addition to a 9-mT magnetic field parallel to the c axis at room temperature. With increasing magnetic field strength perpendicular to the c axis, the signal amplitude of the peak P_3^{1a} (due to spin transition $3/2 \leftrightarrow 1/2$) falls rapidly compared to the peak P_3^{1b} (due to the spin transition $-3/2 \leftrightarrow -1/2$). At around 4.7 mT, the signal amplitude of the peak P_3^{1a} is almost zero, but the signal for P_3^{1b} remains. With further increase of the perpendicular magnetic field strength P_{1a}^3 amplitude becomes negative. The intensity pattern of the multi-photon peaks is also similar to peaks $P_{i=2,3}^{1a(b)}$. Figure 12(b) shows the simulated ODMR recorded in different magnetic fields $\perp$ to the c axis along with 9 mT magnetic field parallel to the c axis. The RF strength Ω_1 used for both vacancies was 2 MHz. In the simulations, we did not consider the effect of the magnetic field on the excited and shelving states of the silicon-vacancy, which can change the optical pumping scheme. Instead of equally populating ground state spin levels

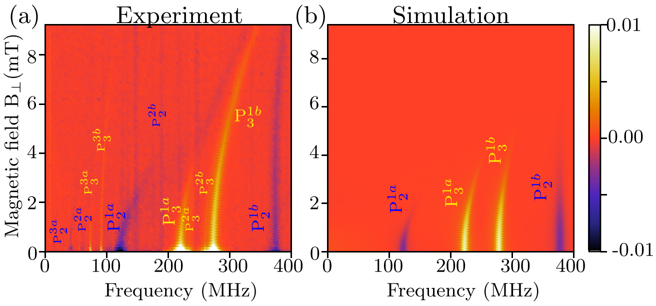

FIG. 12. (a) Experimental and (b) simulated ODMR in 9 mT $\parallel$ c axis along with sweeping magnetic field $\perp$ c axis.

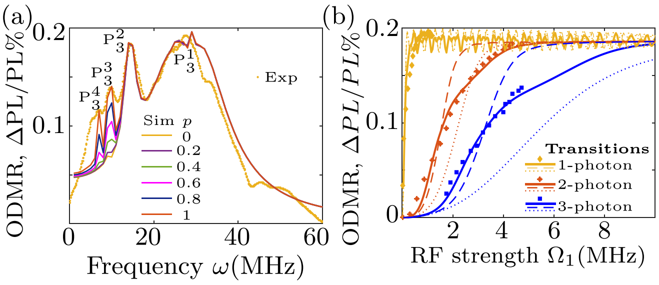

FIG. 13. (a) Experimental and simulated CW-ODMR plots for V_3 with the RF Hamiltonian of Eq. (8). (b) Amplitudes of the different peaks vs RF strength. Diamonds, stars, and squares represent experimentally measured data. Dotted, dashed, and solid curves are the simulations obtained by solving Eq. (7) numerically for different photons transitions with RF Hamiltonian given Eq. (8) with $p = 0$, $= 1$, and $= 1$ along with consideration of the RF inhomogeneity, respectively.

$\pm 1/2$, the spin level $-1/2$ gets slightly more populated; this could be the reason for the difference between the simulated and experimental intensity variation of peaks P_3^{1b} and P_2^{1b} with perpendicular magnetic.

C. RF field with a component parallel to the *c* axis

In the CW-ODMR experiments, we generate the RF field with a wire terminated by a 50-W attenuator with 50 Ω resistance. The resulting RF Hamiltonian includes a component of the magnetic field parallel to the z axis (c axis), which is usually ignored due to its negligible effect on 1 RF photon absorption transitions. However, with the relatively strong fields considered here, its effect can not be neglected, as we show here. Figure 13(a) shows the experimental and simulated CW-ODMR spectra for V_3. The method used to simulate these plots is the same as explained in the above Sec. IV C except the Hamiltonian used is

$$\mathcal{H}_{\mathrm{RF}}(t) = \Omega_1 \cos(2\pi\omega t)\,(S_x + pS_z), \qquad (8)$$

where $\Omega_1 = 4.7\,\mathrm{MHz}$ and $0 \leqslant p \leqslant 1$. The simulated spectra were also renormalized to match the experimental signal. The ODMR spectrum simulated with $p = 1$ matches well with experimentally measured spectrum. Figure 13(b) compares experimental and simulated amplitudes of the different peaks vs RF field strength. Dotted, dashed and solid curves are the simulations obtained by solving Eq. (7) numerically for different photons transitions with RF Hamiltonian given Eq. (8) with $p = 0$, $= 1$, and $= 1$ along with consideration of the RF inhomogeneity, respectively. To account for the experimental RF inhomogeneity, signals with 0.5, 1, and 1.5 times Ω_1, were calculated and added with weights 0.33, 0.34, and 0.33, respectively. We plot the experimental and simulated data in the same plot using $\Omega_1 = \kappa\sqrt{RF\ POWER}$ with $\kappa = 0.25$ for 1-photon and ≈1 for 2- and 3-photon transitions. Figure 13(b) shows that the z axis RF field strongly affects 2- and 3 RF photons absorption signals, but its effect on 1 RF photons absorption peak is negligible. The experimental data for amplitudes of the different peaks vs RF field strength matches with the solid simulated curves, which also account for the inhomogeneity of the RF field.

VI. DISCUSSION AND CONCLUSIONS

V_{Si}^- in SiC is optically addressable and stores information that can be manipulated using RF coherent control pulses. We studied the silicon vacancies by applying the high-power RF pulses. In the CW-ODMR experiments, we fitted the ODMR signal of 1-, 2-, and 3 RF photons with the square root of the RF power. We applied the maximum possible RF power with the RF amplifier and saturated the 1-, 2-, and 3 RF photons peaks of the V_3 type of vacancy. But for the V_2 kind of vacancy, we can only saturate the 1 RF photon absorption peak. The 1-, 2-, and 3 RF photons absorption peaks fitted well in Eq. (3) with the c value is = 1, 2, and 3. The simulated ODMR Spectra and ODMR signal vs RF coupling strengths show similar dependence.

We measured the Rabi oscillations of V_3 type for the 1-, 2-, and 3 RF photon transitions, which fit well with RF coupling strength $\Omega = 9.1$ MHz for all oscillations, but the dephasing rates differed. The 1 RF photon absorption transition dephase faster than 2 RF photons absorption transition and 2 RF photons absorption transition dephase faster than the 3 RF photons for the same RF power. It can be seen from the CW-ODMR also that the linewidth of 2 RF photons absorption transitions is smaller than the 1 RF photon absorption transitions. We saw very sharp changes in the 3 RF photons absorption Rabi oscillation simulations, but we did not see it in the experiment due to RF inhomogeneity. Further, the simulations of the population dynamics with the σ^- polarized RF field show that the three spin levels $-3/2$, $1/2$, and $-1/2$ were involved in the 2- and 3 RF photons absorption transitions. The populations of spin levels $-3/2$ and $1/2$ were exchanging in 2 RF photons transitions, and for the 3 RF photons transitions, population exchange was between the spin levels $-3/2$, $1/2$, and $-1/2$. With linearly polarized photons, the entire population flip happens between the spin levels only with 1-photon absorption and for the 2- and 3-photon it is RF strength depended. We successfully measured the FID of the V_3 type by exciting it with 1-, 2-, and 3 RF photons.

The magnetic field lifts the degeneracy in the vacancy spin levels, and we can see ODMR peaks for the different transitions. The ODMR recorded in the magnetic field parallel to the c axis clearly shows these different RF photons transitions. The 1 RF photon absorption is transition takes place between the spin levels $\pm 3/2 \leftrightarrow \pm 1/2$ (with high ODMR intensity) and $\mp 3/2 \leftrightarrow \pm 1/2$ (with low ODMR intensity). The 2 RF photons transitions are taking place between the $\mp 3/2 \leftrightarrow \pm 1/2$ and with very low ODMR intensity in spin levels $\pm 3/2 \leftrightarrow \pm 1/2$ also. In the transition $\pm 3/2 \leftrightarrow \pm 1/2$ angular momentum change is ± 2, so angular momentum is conserved for this transition with two RF photons of the same polarization, wherein the other is ± 1, and it is not conserved, giving low intensity. The 3 RF photons absorption transition is taking place between the $\pm 3/2 \leftrightarrow \pm 1/2$. The intensity of these 3 RF photons absorption peaks (P_3^{3a} and P_3^{3b}) is higher than that of the 2 RF photons absorption peaks (P_3^{2a1} and P_3^{2b1}), i.e., transitions between the spin levels $\pm 3/2 \leftrightarrow \pm 1/2$. The higher intensity in 3 RF photons transitions is due to angular momentum conservation, and this could be possible if two out of three RF photons have the same polarization. The ODMR recorded in 9 mT parallel to the c axis and along with the magnetic field perpendicular to the c axis shows the perpendicular magnetic field mixing more the transition $-3/2 \leftrightarrow 1/2$ as compared to the $3/2 \leftrightarrow 1/2$. This effect could be use to prepare a pseudo pure state of V_{Si}^- spin ensemble. Further, the multi-photon transitions depend not only on the amplitude but also on the orientation of the RF field with respect to the symmetry axis of the center.

So, in conclusion, 1, 2, and 3 photons transitions in the negatively charged silicon-vacancy have been observed and characterized. Our results improve the understanding of multi-photon absorption transitions in silicon vacancies and help develop fast quantum coherent control and other applications.

ACKNOWLEDGMENTS

This work was supported by the Deutsche Forschungsgemeinschaft in the frame of the ICRC TRR 160 (Project No. C7) and by RFBR Project No. 19-52-12058.

APPENDIX A: SAMPLE

SiC crystals with a low content of background impurities were grown from a synthesized source. Polycrystalline sources were synthesized from semiconductor silicon and spectrally pure carbon. Polycrystalline silicon and spectrally pure graphite in the form of powder were chosen as the powder. Before the synthesis, the crucible and internal furnace reinforcement were degassed at a temperature of 220 °C and a vacuum of 10^{-3} torrs for 2 hours by resistive heating growth machine, after which the crucible was loaded with a mixture of carbon and silicon powders in a stoichiometric ratio. The process of manufacturing silicon carbide powder was carried out in a vacuum. To make the crucible, graphite was used with a minimum content of background impurities, such as Mersen 6516PT. In addition, it should be noted that all parts of the crucible must be made of the same brand of graphite in order to exclude the destruction of parts due to the difference in the coefficients of thermal expansion of materials when the crucible was heated to the synthesis temperature of the source (above 1600 °C). As a seed, a silicon carbide crystal of polytype 6H was used orientation on-axis. Crystal growth parameters: Temperature 2050 °C, argon pressure about 2–5 torr, high-purity argon 99.9999%, growth rate about 150 μm/h. The micropore density in the grown crystal does not exceed 3 cm^{-2}. For creating silicon vacancies, the crystal was irradiated with electrons with a dose of 10^{18} cm^{-2} and an energy of 2 MeV at room temperature.

APPENDIX B: ODMR SETUP

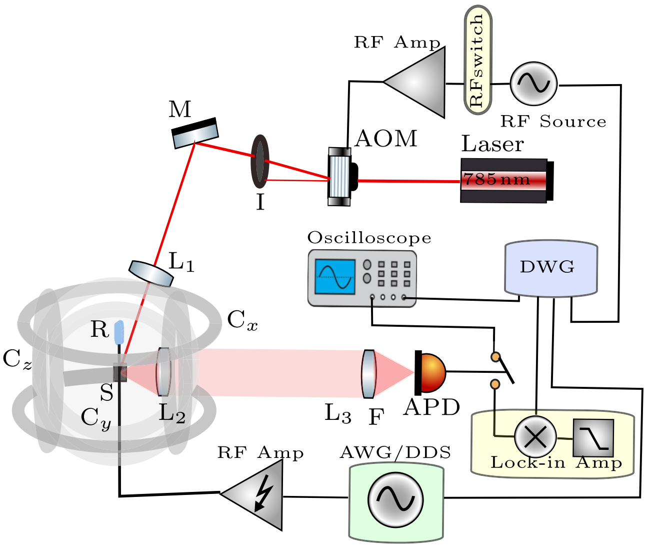

FIG. 14. Experimental setup used for the ODMR experiments. An acoustic-optical modulator (labeled AOM) is used to generate laser light pulses. Mirror, lenses, iris, and 850-nm long-pass filter are labeled M, L, I, and F. An avalanche photodiode (APD) converts the PL signal into an electrical signal. Three orthogonal sets of Helmholtz coils labeled C_x, C_y, and C_z are used to apply a magnetic field in an arbitrary direction.

Figure 14 shows the setup used for the cw- and time-resolved ODMR measurements, which is also used in our previous papers [9,10]. We used a 785-nm diode laser as our light source [a laser diode (Thorlabs LD785-SE400), a laser diode controller (LDC202C series) and a temperature controller (TED 200C)]. An acousto-optical modulator (NEC model OD8813A) was used for creating the laser light pulses. For applying the static magnetic field to the sample, we used three orthogonal coil-pairs. The PL signal was recorded with an avalanche photodiode (APD) module (C12703 series from Hamamatsu). The signal from the APD was recorded with the USB oscilloscope card (PicoScope 2000 series) during pulse mode ODMR experiments. For cw-ODMR, the signal from APD was recorded with the lock-in (SRS model SR830 DSP). An RF source, we used a direct digital synthesizer (DDS) AD9915 from Analog Devices. An RF signal from the source was amplified using an RF amplifier (LZY-22+ from mini circuits and ZHL-5W-1+). This amplified RF power feed to the sample with a 50 μm diameter wire terminated with a 50-ohm resistor via a 50 W attenuator. For pulsed ODMR experiments, we used an arbitrary wave generator (AWG)(DAx14000 from Hunter Micro). An RF signal from the source was amplified using an RF amplifier (LZY-22+ from mini circuits). This amplified RF power was applied to the sample with a Helmholtz-pair of RF coils with a diameter of 2.5 mm terminated with a 50-ohm resistor. We used a digital word generator (DWG; SpinCore PulseBlaster ESR-PRO PCI card) to generate TTL (transistor transistor logic) pulses that trigger the laser RF pulses.

APPENDIX C: LINDBLAD OPERATORS

Lindblad operators used in the Lindblad equation (7) for including the optical pumping process of the V_3 type of vacancy:

$$L_1 = \sqrt{\delta}\begin{pmatrix} 0 & 0 & 0 & 0 \\ 1 & 0 & 0 & 0 \\ 0 & 0 & 0 & 0 \\ 0 & 0 & 0 & 0 \end{pmatrix}$$

,

$$L_2 = \sqrt{\delta}\begin{pmatrix} 0 & 0 & 0 & 0 \\ 0 & 0 & 0 & 1 \\ 0 & 0 & 0 & 0 \\ 0 & 0 & 0 & 0 \end{pmatrix}$$

,

$$L_3 = \sqrt{\delta}\begin{pmatrix} 0 & 0 & 0 & 0 \\ 0 & 0 & 0 & 0 \\ 1 & 0 & 0 & 0 \\ 0 & 0 & 0 & 0 \end{pmatrix}$$

,

$$L_4 = \sqrt{\delta}\begin{pmatrix} 0 & 0 & 0 & 0 \\ 0 & 0 & 0 & 0 \\ 0 & 0 & 0 & 1 \\ 0 & 0 & 0 & 0 \end{pmatrix}$$

,

$$L_5 = \sqrt{\delta}\begin{pmatrix} 0 & 0 & 0 & 0 \\ 0 & 0 & 1 & 0 \\ 0 & 1 & 0 & 0 \\ 0 & 0 & 0 & 0 \end{pmatrix}$$

,

Lindblad operators used for including the optical pumping process of the V_2 type of vacancy:

$$L_1 = \sqrt{\delta}\begin{pmatrix} 0 & 1 & 0 & 0 \\ 0 & 0 & 0 & 0 \\ 0 & 0 & 0 & 0 \\ 0 & 0 & 0 & 0 \end{pmatrix}$$

,

$$L_2 = \sqrt{\delta}\begin{pmatrix} 0 & 0 & 0 & 0 \\ 0 & 0 & 0 & 0 \\ 0 & 0 & 0 & 0 \\ 0 & 1 & 0 & 0 \end{pmatrix}$$

,

$$L_3 = \sqrt{\delta}\begin{pmatrix} 0 & 0 & 1 & 0 \\ 0 & 0 & 0 & 0 \\ 0 & 0 & 0 & 0 \\ 0 & 0 & 0 & 0 \end{pmatrix}$$

,

$$L_4 = \sqrt{\delta}\begin{pmatrix} 0 & 0 & 0 & 0 \\ 0 & 0 & 0 & 0 \\ 0 & 0 & 0 & 0 \\ 0 & 0 & 1 & 0 \end{pmatrix}$$

,

$$L_5 = \sqrt{\delta}\begin{pmatrix} 0 & 0 & 0 & 1 \\ 0 & 0 & 0 & 0 \\ 0 & 0 & 0 & 0 \\ 1 & 0 & 0 & 0 \end{pmatrix}$$

.

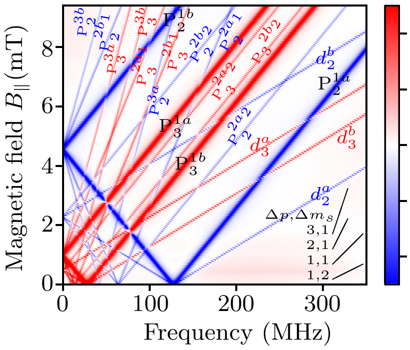

FIG. 15. Plot showing different possible transitions for the V_1/V_3 and V_2 for a range of magnetic fields B ∥ c axis, calculated using eigenvalues of Hamiltonian given in Eq. (1). Peaks labeled with $P_2^{1a(b)}$ ($P_3^{1a(b)}$), $P_2^{2a(b)}$ ($P_3^{2a(b)}$) and $P_2^{3a(b)}$ ($P_3^{3a(b)}$) are 1-, 2-, and 3, RF photons absorption peaks due to the single quantum spin transition $\Delta m_s = 1$, where peaks $d_2^{a(b)}(d_3^{a(b)})$ are 1 RF photon absorption peaks due to double quantum spin transition $\Delta m_s = 2$ for $V_2(V_3)$ type of V_{Si}^-. Slope of different transitions are depends on the number RF photon absorb Δp and the change in the spin quantum number Δm_s during the transitions.

Lindblad operators for including the relaxation contribution $L_6 = \sqrt{2\beta}\, S_z$, $L_7 = \sqrt{2\alpha}\, S_x$, where $S_z = \frac{1}{2}\begin{pmatrix} 3 & 0 & 0 & 0 \\ 0 & 1 & 0 & 0 \\ 0 & 0 & -1 & 0 \\ 0 & 0 & 0 & -3 \end{pmatrix}$ and $S_x = \frac{1}{2}\begin{pmatrix} 0 & \sqrt{3} & 0 & 0 \\ \sqrt{3} & 0 & 2 & 0 \\ 0 & 2 & 0 & \sqrt{3} \\ 0 & 0 & \sqrt{3} & 0 \end{pmatrix}$.

The values of k_i are used to solve Eq. (7) with the Runge-Kutta 4 method:

(i) $k_1 = -i(\mathcal{H}_t(t_n).\rho(n) - \rho(n).\mathcal{H}_t(t_n)) + \sum_{\alpha,\beta,\delta} L_i^\dagger.\rho(n).L_i - \frac{1}{2}(L_i^\dagger L_i.\rho(n) + \rho(n).L_i^\dagger L_i)$;

(ii) $k_2 = -i(\mathcal{H}_t(\frac{\Delta t}{2} + t_n).(\frac{\Delta t k_1}{2} + \rho_n) - (\frac{\Delta t k_1}{2} + \rho_n).\mathcal{H}_t(\frac{\Delta t}{2} + t_n)) + \sum_{\alpha,\beta,\delta} L_i.(\frac{\Delta t k_1}{2} + \rho_n).L_i^\dagger - \frac{1}{2}((\frac{\Delta t k_1}{2} + \rho_n).L_i^\dagger L_i + L_i^\dagger L_i.(\frac{\Delta t k_1}{2} + \rho_n))$;

(iii) $k_3 = -i(\mathcal{H}_t(\frac{\Delta t}{2} + t_n).(\frac{\Delta t k_2}{2} + \rho_n) - (\frac{\Delta t k_2}{2} + \rho_n).\mathcal{H}_t(\frac{\Delta t}{2} + t_n)) + \sum_{\alpha,\beta,\delta} L_i.(\frac{\Delta t k_2}{2} + \rho_n).L_i^\dagger - \frac{1}{2}((\frac{\Delta t k_2}{2} + \rho_n).L_i^\dagger L_i + L_i^\dagger L_i.(\frac{\Delta t k_2}{2} + \rho_n))$;

(iv) $k_4 = -i(\mathcal{H}_t(\Delta t + t_n).(\Delta t\, k_3 + t_n) - (\Delta t\, k_3 + \rho_n).\mathcal{H}_t(\Delta t + t_n)) + \sum_{\alpha,\beta,\delta} L_i^\dagger.(\Delta t\, k_3 + \rho_n).L_i - \frac{1}{2}((\Delta\, t k_3 + \rho_n).L_i^\dagger L_i + L_i^\dagger L_i.(\Delta t\, k_3 + \rho_n))$;

$\rho_{n+1} = \rho_n + \frac{1}{6}\Delta t(k_1 + 2k_2 + 2k_3 + k_4)$;

Figure 15 shows different possible transitions for the V_1/V_3 and V_2 for a range of magnetic fields B ∥ c axis, calculated using eigenvalues of Hamiltonian given in Eq. (1). Red and blue color lines represent the possible 1-, 2-, and 3 RF photon absorption transitions.

---

[1] V. A. Soltamov, C. Kasper, A. V. Poshakinskiy, A. N. Anisimov, E. N. Mokhov, A. Sperlich, S. A. Tarasenko, P. G. Baranov, G. V. Astakhov, and V. Dyakonov, Excitation and coherent control of spin qudit modes in silicon carbide at room temperature, Nat. Commun. **10**, 1678 (2019).

[2] M. Widmann, S.-Y. Lee, T. Rendler, N. T. Son, H. Fedder, S. Paik, L.-P. Yang, N. Zhao, S. Yang, I. Booker *et al.*, Coherent control of single spins in silicon carbide at room temperature, Nat. Mater. **14**, 164 (2015).

[3] D. M. Lukin, M. A. Guidry, and J. Vučković, Integrated quantum photonics with silicon carbide: Challenges and prospects, PRX Quantum **1**, 020102 (2020).

[4] P. G. Baranov, A. P. Bundakova, A. A. Soltamova, S. B. Orlinskii, I. V. Borovykh, R. Zondervan, R. Verberk, and J. Schmidt, Silicon vacancy in SiC as a promising quantum system for single-defect and single-photon spectroscopy, Phys. Rev. B **83**, 125203 (2011).

[5] C. Babin, R. Stöhr, N. Morioka, T. Linkewitz, T. Steidl, R. Wörnle, D. Liu, E. Hesselmeier, V. Vorobyov, A. Denisenko *et al.*, Fabrication and nanophotonic waveguide integration of silicon carbide colour centres with preserved spin-optical coherence, Nat. Mater. **21**, 67 (2021).

[6] D. J. Christle, A. L. Falk, P. Andrich, P. V. Klimov, J. U. Hassan, N. T. Son, E. Janzén, T. Ohshima, and D. D. Awschalom, Isolated electron spins in silicon carbide with millisecond coherence times, Nat. Mater. **14**, 160 (2015).

[7] A. L. Falk, B. B. Buckley, G. Calusine, W. F. Koehl, V. V. Dobrovitski, A. Politi, C. A. Zorman, P. X.-L. Feng, and D. D. Awschalom, Polytype control of spin qubits in silicon carbide, Nat. Commun. **4**, 1819 (2013).

[8] H. Kraus, V. Soltamov, D. Riedel, S. Väth, F. Fuchs, A. Sperlich, P. Baranov, V. Dyakonov, and G. Astakhov, Room-temperature quantum microwave emitters based on spin defects in silicon carbide, Nat. Phys. **10**, 157 (2014).

[9] H. Singh, A. N. Anisimov, I. D. Breev, P. G. Baranov, and D. Suter, Optical spin initialization of spin-$\frac{3}{2}$ silicon vacancy centers in $6H-$SiC at room temperature, Phys. Rev. B **103**, 104103 (2021).

[10] H. Singh, A. N. Anisimov, S. S. Nagalyuk, E. N. Mokhov, P. G. Baranov, and D. Suter, Experimental characterization of spin-3/2 silicon vacancy centers in $6H$-SiC, Phys. Rev. B **101**, 134110 (2020).

[11] V. A. Soltamov, B. V. Yavkin, A. N. Anisimov, H. Singh, A. P. Bundakova, G. V. Mamin, S. B. Orlinskii, E. N. Mokhov, D. Suter, and P. G. Baranov, Relaxation processes and high-field coherent spin manipulation in color center ensembles in $6H$-SiC, Phys. Rev. B **103**, 195201 (2021).

[12] E. Sörman, N. T. Son, W. M. Chen, O. Kordina, C. Hallin, and E. Janzén, Silicon vacancy related defect in 4H and 6H SiC, Phys. Rev. B **61**, 2613 (2000).

[13] T. Biktagirov, W. G. Schmidt, U. Gerstmann, B. Yavkin, S. Orlinskii, P. Baranov, V. Dyakonov, and V. Soltamov, Polytypism driven zero-field splitting of silicon vacancies in $6H$-SiC, Phys. Rev. B **98**, 195204 (2018).

[14] J. Davidsson, V. Ivády, R. Armiento, T. Ohshima, N. T. Son, A. Gali, and I. A. Abrikosov, Identification of divacancy and silicon vacancy qubits in 6H-SiC, Appl. Phys. Lett. **114**, 112107 (2019).

[15] I. D. Breev, Z. Shang, A. V. Poshakinskiy, H. Singh, Y. Berencén, M. Hollenbach, S. S. Nagalyuk, E. N. Mokhov, R. A. Babunts, P. G. Baranov, D. Suter, S. A. Tarasenko, G. V. Astakhov, and A. N. Anisimov, Inverted fine structure of a $6H$-SiC qubit enabling robust spin-photon interface, npj Quantum Inf. **8**, 23 (2022).

[16] K. R. K. Rao and D. Suter, Nonlinear dynamics of a two-level system of a single spin driven beyond the rotating-wave approximation, Phys. Rev. A **95**, 053804 (2017).

[17] L. Childress and J. McIntyre, Multifrequency spin resonance in diamond, Phys. Rev. A **82**, 033839 (2010).

[18] J. Meinel, V. Vorobyov, B. Yavkin, D. Dasari, H. Sumiya, S. Onoda, J. Isoya, and J. Wrachtrup, Heterodyne sensing of microwaves with a quantum sensor, Nat. Commun. **12**, 2737 (2021).

[19] S. Ashhab, J. R. Johansson, A. M. Zagoskin, and F. Nori, Two-level systems driven by large-amplitude fields, Phys. Rev. A **75**, 063414 (2007).

[20] Y. Zur, M. H. Levitt, and S. Vega, Multiphoton NMR spectroscopy on a spin system with $\mathrm{i} = 1/2$, J. Chem. Phys. **78**, 5293 (1983).

[21] V. Nathan, A. H. Guenther, and S. S. Mitra, Review of multiphoton absorption in crystalline solids, J. Opt. Soc. Am. B **2**, 294 (1985).

[22] R. F. Wallis, J. J. Brion, E. Burstein, and A. Hartstein, Theory of surface polaritons in anisotropic dielectric media with application to surface magnetoplasmons in semiconductors, Phys. Rev. B **9**, 3424 (1974).

[23] D. Hutchings and E. W. Van Stryland, Nondegenerate two-photon absorption in zinc blende semiconductors, J. Opt. Soc. Am. B **9**, 2065 (1992).

[24] A. Hayat, P. Ginzburg, and M. Orenstein, Observation of two-photon emission from semiconductors, Nat. Photonics **2**, 238 (2008).

[25] A. Pines, S. Vega, and M. Mehring, NMR double-quantum spin decoupling in solids, Phys. Rev. B **18**, 112 (1978).

[26] S. G. Carter, O. O. Soykal, P. Dev, S. E. Economou, and E. R. Glaser, Spin coherence and echo modulation of the silicon vacancy in $4H-$SiC at room temperature, Phys. Rev. B **92**, 161202(R) (2015).

[27] D. Simin, V. A. Soltamov, A. V. Poshakinskiy, A. N. Anisimov, R. A. Babunts, D. O. Tolmachev, E. N. Mokhov, M. Trupke, S. A. Tarasenko, A. Sperlich, P. G. Baranov, V. Dyakonov, and G. V. Astakhov, All-Optical dc Nanotesla Magnetometry Using Silicon Vacancy Fine Structure in Isotopically Purified Silicon Carbide, Phys. Rev. X **6**, 031014 (2016).

[28] V. A. Soltamov, A. A. Soltamova, P. G. Baranov, and I. I. Proskuryakov, Room Temperature Coherent Spin Alignment of Silicon Vacancies in $4H$- and $6H$-SiC, Phys. Rev. Lett. **108**, 226402 (2012).

[29] D. Carbonera, Optically detected magnetic resonance (ODMR) of photoexcited triplet states, Photosynth. Res. **102**, 403 (2009).

[30] D. Suter, Optical detection of magnetic resonance, Magn. Reson. **1**, 115 (2020).

[31] D. Suter and F. Jelezko, Single-spin magnetic resonance in the nitrogen-vacancy center of diamond, Prog. Nucl. Magn. Reson. Spectrosc. **98-99**, 50 (2017).

[32] M. E. Bathen and L. Vines, Manipulating single-photon emission from point defects in diamond and silicon carbide, Adv. Quantum Technol. **4**, 2100003 (2021).

[33] A. Abragam, *The Principles of Nuclear Magnetism* (Oxford University Press, Oxford, 1961).

[34] R. Nagy, M. Niethammer, M. Widmann, Y.-C. Chen, P. Udvarhelyi, C. Bonato, J. U. Hassan, R. Karhu, I. G. Ivanov, N. T. Son *et al.*, High-fidelity spin and optical control of single silicon-vacancy centres in silicon carbide, Nat. Commun. **10**, 1954 (2019).

[35] D. V. Sosnovsky and K. L. Ivanov, Level-crossing induced spin phenomena in SiC: A theoretical study, Phys. Rev. B **103**, 014403 (2021).